POLITECNICO DI TORINO
Repository ISTITUZIONALE

Silver Electrodes Are Highly Selective for CO in CO2 Electroreduction due to Interplay between Voltage Dependent Kinetics and Thermodynamics

Original
Silver Electrodes Are Highly Selective for CO in CO2 Electroreduction due to Interplay between Voltage Dependent Kinetics and Thermodynamics / Re Fiorentin, M., Risplendi, F., Salvini, C., Zeng, J., Cicero, G., Jónsson, H.. - In: THE JOURNAL OF PHYSICAL CHEMISTRY LETTERS. - ISSN 1948-7185. - 15:46(2024), pp. 11538-11545. [10.1021/acs.jpclett.4c02869]

Availability:
This version is available at: 11583/2995253 since: 2024-12-12T13:58:01Z

Publisher:
American Chemical Society

Published
DOI:10.1021/acs.jpclett.4c02869

Terms of use:

This article is made available under terms and conditions as specified in the corresponding bibliographic description in the repository

Publisher copyright

(Article begins on next page)

29 November 2026

THE JOURNAL OF PHYSICAL CHEMISTRY LETTERS
A JOURNAL OF THE AMERICAN CHEMICAL SOCIETY

pubs.acs.org/JPCL

Letter

Silver Electrodes Are Highly Selective for CO in CO_2 Electroreduction due to Interplay between Voltage Dependent Kinetics and Thermodynamics

Michele Re Fiorentin,[†] Francesca Risplendi,[†] Clara Salvini, Juqin Zeng, Giancarlo Cicero, and Hannes Jónsson*

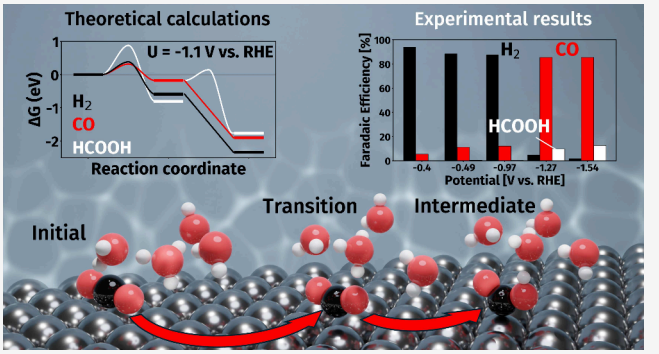
Cite This: *J. Phys. Chem. Lett.* 2024, 15, 11538−11545

Read Online

ACCESS | Metrics & More | Article Recommendations | Supporting Information

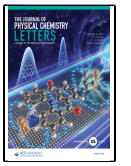
Downloaded via POLITECNICO DI TORINO on December 12, 2024 at 13:48:28 (UTC).
See https://pubs.acs.org/sharingguidelines for options on how to legitimately share published articles.

ABSTRACT: Electrochemical reduction is a promising way to make use of CO_2 as feedstock for generating renewable fuel and valuable chemicals. Several metals can be used as the electrocatalyst to generate CO and formic acid, but hydrogen formation is an unwanted side reaction that can even be dominant. The lack of selectivity is, in general, a significant problem, but silver-based electrocatalysts have been shown to be highly selective, with faradaic efficiency of CO production exceeding 90%, when the applied voltage is below −1 V vs RHE. In this voltage range, only a small amount of hydrogen and formate is formed. We present calculations of the activation free energy for the various elementary steps as a function of applied voltage at the three low index facets, Ag(111), Ag(100) and Ag(110), as well as experimental measurements on polycrystalline electrodes, to identify the reason for this high selectivity. The formation of formic acid is suppressed, even though it is thermodynamically favored, because of the low coverage of adsorbed hydrogen and kinetic hindrance to the formation of the HCOO* intermediate, while *COOH, a key intermediate in CO formation, is thermodynamically unstable until the applied voltage reaches −1 V vs RHE, at which point the kinetics for its formation are more favorable than for hydrogen. The calculated results are consistent with experimental measurements carried out for acidic conditions and provide an atomic scale insight into the high CO selectivity of silver-based electrocatalysts.



In the pursuit of carbon neutrality, a key strategy entails balancing emissions by capturing anthropogenic carbon dioxide and converting it into valuable products. One of the most promising transformative approach relies on the electrochemical reduction of carbon dioxide using engineered electrocatalysts capable of efficiently enhancing reaction kinetics, controlling reaction pathways, influencing product selectivity, and ensuring stability under working conditions.[1,2] A wide range of electrocatalysts have been proposed so far for the CO_2 reduction reaction (CO_2RR).[3−10] The choice of a specific catalyst determines the primary product of the reduction, which can vary from formate/formic acid or CO, generated through a $2e^-$ reduction, to multielectron transfer products like alcohols and hydrocarbons. Additionally, the presence of competing reactions, such as the hydrogen evolution reaction (HER), significantly influences the catalyst selectivity. The complex mechanisms involved in electrochemical reactions depend upon several factors[11,12] such as the morphology of the electrocatalyst,[13−15] the composition of the electrolyte,[16−18] its pH,[12,19] the CO_2 partial pressure,[12,20] the cell dimensions,[21] and, crucially, the applied potential. The impact of these factors on CO_2RR can be assessed and predicted through theoretical modeling based on atomistic simulations. In particular, Density Functional Theory (DFT) provides valuable insight on the reaction mechanisms, enhancing our understanding of both the thermodynamics and kinetics of CO_2RR. The DFT thermochemical model (TCM)[22] of electrocatalytic reactions has proven to be a robust method for predicting central thermodynamic quantities. It can provide key understanding and predictions of CO_2RR mechanisms that closely align with experimental observations and enable detailed examinations of the free energy landscape.[23−25] However, by focusing solely on reaction thermodynamics, the TCM can only provide a lower bound on the reaction overpotential. More recently, efforts have been made to address the challenge of modeling and computing

Received: October 3, 2024
Revised: November 4, 2024
Accepted: November 5, 2024
Published: November 11, 2024



ACS Publications
© 2024 American Chemical Society

activation energies in electrochemical reactions. Several studies[26−33] have investigated the kinetics of CO_2RR on metallic surfaces, offering additional insight and introducing a fundamental perspective on the problem that was previously missing.

In this Letter, we investigate the selectivity of silver surfaces toward CO_2RR at varying applied potential. We show that a combined theoretical study, encompassing both thermodynamics and kinetics, can fully clarify some crucial aspects of the behavior of silver electrocatalysts that still lack a fundamental explanation. Silver-based electrocatalysts are widely employed in the electrocatalytic conversion of CO_2 to CO,[34−36] thanks to their remarkable selectivity. They achieve Faradaic efficiencies (FEs) for CO production exceeding 90% and current densities suitable for industrial scale, reaching over 150 mA/cm^2.[34−38] The production of HCOOH is observed in minimal quantities across varying applied potentials. Experimental evidence[39−42] shows that the selectivity switches at intermediate overpotentials. Hydrogen evolution is favored at applied potentials $U \gtrsim -0.9$ V vs RHE. As the bias is lowered, CO replaces H_2 as the favored product, accompanied by an increase in the current density. A further change occurs at more cathodic potentials, when the FE of CO production drops significantly and the electrocatalyst selectivity switches back to HER. The analysis of the experimental current densities suggested that, unlike the former, this latter switch in selectivity can be attributed to mass transfer limitations.[42] While well-known experimentally, the fundamental mechanisms behind this evident competition between CO and H_2 production at varying applied bias, as well as the extremely low formate production have not been extensively explored by atomistic modeling. In our DFT study of various CO_2RR pathways, along with the competing HER, we find that while HCOO*, critical for formic acid production, is the most thermodynamically stable reaction intermediate, it is kinetically unfavorable across all applied biases. Crucially, we show that the selectivity crossover between CO and H_2 production at intermediate potentials emerges only from a delicate interplay between reaction thermodynamics and kinetics.

Three crystal surfaces, namely (111), (100) and (110) were considered to model the silver electrode. We performed DFT electronic structure calculations with the VASP code,[43−46] following the constant-potential computational setup established in refs 28 and 29 The Kohn−Sham equations were solved using the PAW[47] method and the RPBE functional,[48] with Monkhorst−Pack grids for Brillouin zone integrations.[49,50] Explicit H_2O molecules and the GLSSA13 implicit solvent model,[51] as implemented in the VASPsol[52−54] plugin, were included to account for solvation effects. The implicit solvent model allows for the addition to the cell of a fractional number of electrons, compensated by the implicit counterion distribution. By varying the number of electrons in the DFT calculations it is possible to adjust the potential of the silver slab, obtained from its workfunction referenced to the bulk electrolyte. Standard conversions were then performed to obtain electrode potentials with respect to the RHE. The implicit solvent model assumes a bulk dielectric constant of water ϵ_{bulk} = 78.4 and a Debye length of 3 Å, corresponding to 1 M concentration of a monovalent symmetrical electrolyte. This is in line with the strong acidic conditions that we plan to study. Transition structures (TSs) were found as first-order saddle points along the minimum-energy path by means of nudged elastic band calculations followed by minimum-mode following[55−58] at constant potential. For further computational details, we refer the reader to the Supporting Information.

A first thermodynamic study was performed to evaluate the Gibbs free energy of the first reaction steps of CO_2RR and HER via standard TCM. Specifically, we considered the two alternative proton-coupled electron transfer (PCET) reaction paths of CO_2RR, where CO_2 is reduced to either CO through the *COOH intermediate

$$* + CO_2 \xrightarrow{H^+ + e^-} *COOH \quad (1)$$

$$*COOH \xrightarrow{H^+ + e^-} CO + H_2O \quad (2)$$

or to HCOOH through the HCOO* intermediate

$$* + CO_2 \xrightarrow{H^+ + e^-} HCOO* \quad (3)$$

$$HCOO* \xrightarrow{H^+ + e^-} HCOOH \quad (4)$$

From Figure 1, reporting the Gibbs free energies of formation calculated on the three silver surfaces, we can notice that the

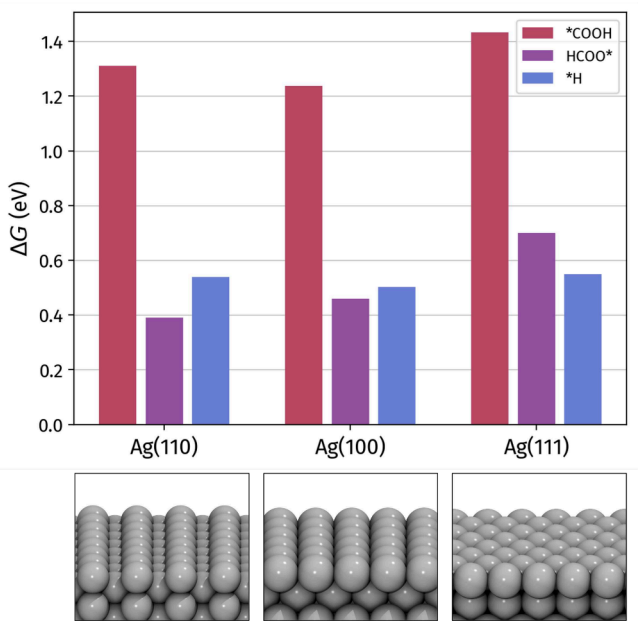


Figure 1. Gibbs free energies of formation of *COOH (red bars), HCOO* (purple bars) and *H (blue bars) computed with the TCM. From left to right: Ag(110), Ag(100) and Ag(111) surfaces.

formation of *COOH, eq 1, is thermodynamically less favored than that of HCOO*, eq 3, on all silver surfaces. Interestingly, the Gibbs free energy of HCOO* formation increases in the order Ag(110) < Ag(100) < Ag(111), as the degree of surface packing increases and the atoms at the surface are less undercoordinated. Finally, we also considered HER, through the successive Volmer and Heyrovsky steps, as

$$* \xrightarrow{H^+ + e^-} *H \quad (5)$$

$$*H \xrightarrow{H^+ + e^-} H_2 \quad (6)$$

Figure 1 shows that the formation of *H is disfavored compared to HCOO* on all surfaces, except for Ag(111), where hydrogen is adsorbed on the fcc site with higher stability. The results of this preliminary analysis confirm

https://doi.org/10.1021/acs.jpclett.4c02869
J. Phys. Chem. Lett. 2024, 15, 11538−11545

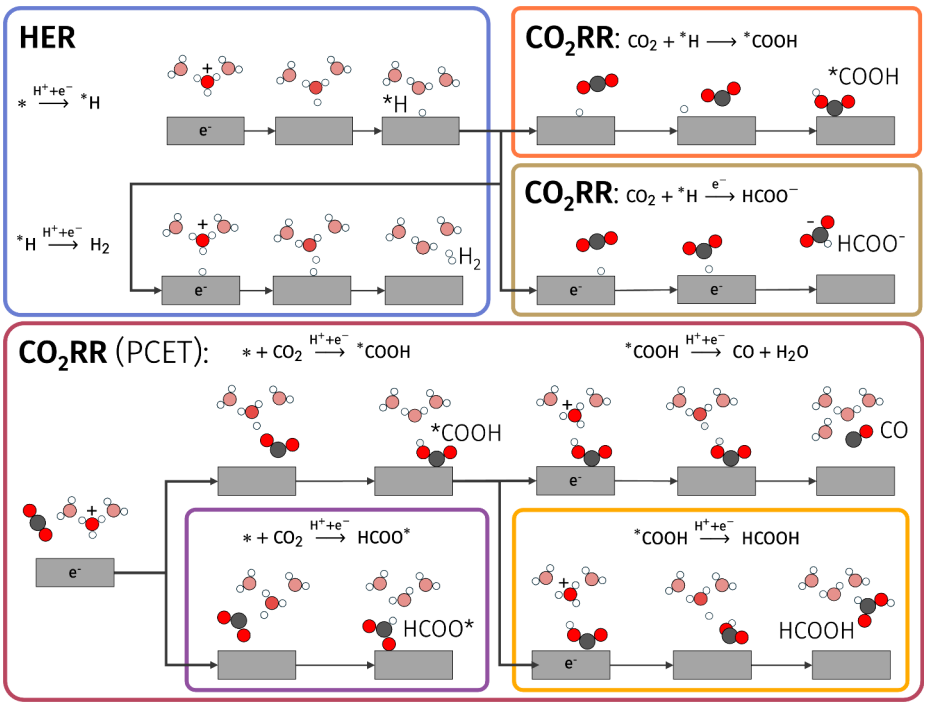


Figure 2. Diagram of the studied reaction pathways, TSs and intermediate states for CO_2RR and HER. Carbon, oxygen and hydrogen atoms are represented by black, red and white circles, respectively. Gray rectangles represent the silver slab.

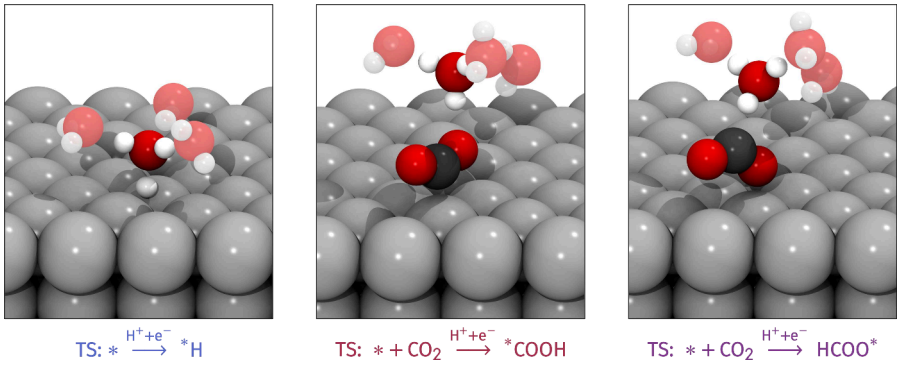


Figure 3. Geometries of three representative TSs on Ag(111) at $U = -0.8$ V vs RHE. Left panel: HER step in eq 5. Central panel: CO_2RR step in eq 1. Right panel: CO_2RR step in eq 3. Carbon, oxygen, hydrogen and silver atoms are represented by black, red, white and gray spheres, respectively. Lighter colors are used to mark spectator water molecules.

previous theoretical findings: based on reaction thermodynamics, silver electrodes should be expected to produce HCOOH and H_2, contrary to what is observed experimentally.[39,42,59,60] Clearly, the TCM alone cannot reliably predict the selectivity of Ag surfaces and a more comprehensive investigation, incorporating explicitly applied potentials and TS searches, is necessary.

We identified the TSs relevant to CO_2RR and HER under constant external potential, obtaining the corresponding activation grand-canonical energy,[28] $\Delta\Omega^{\ddagger}$. In this study, we focus on the kinetics of reactions occurring in acidic conditions, where the proton donors are solvated hydronium ions, H_3O^+. We also assume efficient mass transport, ensuring that the hydronium concentration remains sufficiently high at the interface to suppress reactions involving water as the proton donor. This condition is indeed achieved in our experimental setup (see Supporting Information).

The studied reaction pathways, TSs and intermediate states are reported in the scheme in Figure 2. Beside the PCET reaction in eq 1, the *COOH intermediate can be obtained from a CO_2 molecule and a surface-adsorbed hydrogen atom, as

$$CO_2 + {}^*H \rightarrow {}^*COOH \tag{7}$$

Similarly, CO_2 can be also directly transformed into $HCOO^-$ with an adsorbed *H and a transferred electron, as

$$CO_2 + {}^*H \xrightarrow{e^-} HCOO^- \tag{8}$$

$HCOO^-$ then readily transforms into HCOOH in a strongly acidic environment. Finally, formic acid can also be obtained from the *COOH intermediate as

$$^*COOH \xrightarrow{H^+ + e^-} HCOOH \tag{9}$$

The geometries of three representative TSs on Ag(111) at $U = -0.8$ V vs RHE are shown in Figure 3. The geometries of the other investigated TSs are reported in the Supporting Information. The $\Delta\Omega^{\ddagger}$s at the three studied potentials, $U =$

https://doi.org/10.1021/acs.jpclett.4c02869
J. Phys. Chem. Lett. 2024, 15, 11538−11545

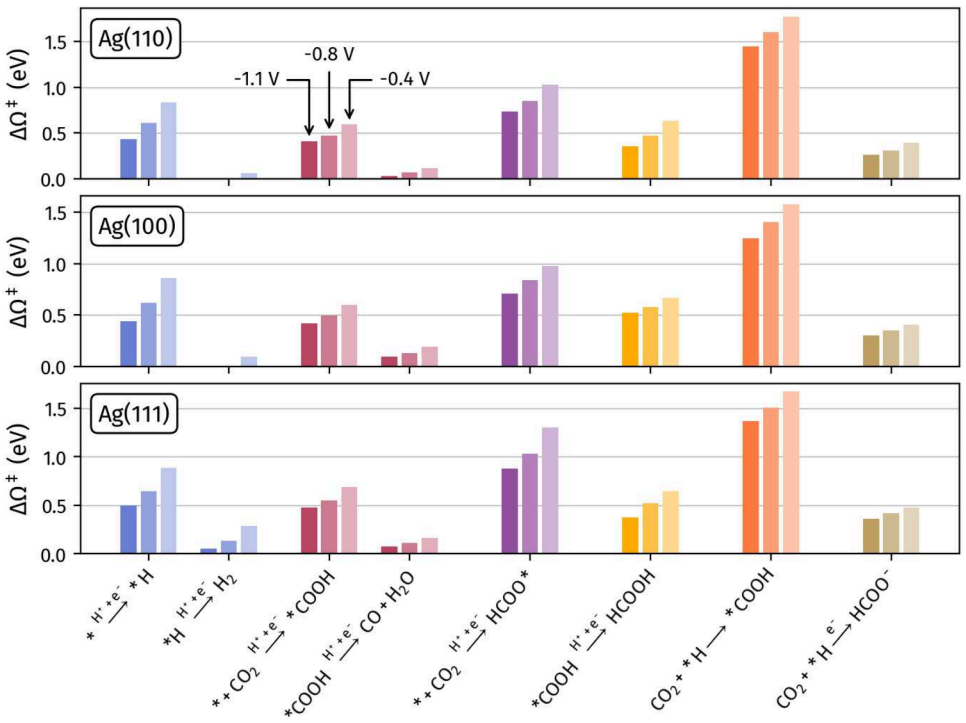


Figure 4. Grand-canonical activation energies $\Delta\Omega^{\ddagger}$ of the studied steps of HER and CO_2RR. Top to bottom: Ag(110), Ag(100) and Ag(111) surfaces. Each group represents a reaction step and consists of three bars, corresponding to the three studied potentials, arranged from left to right (darker to lighter shades): $U = -1.1, -0.8, -0.4$ V vs RHE.

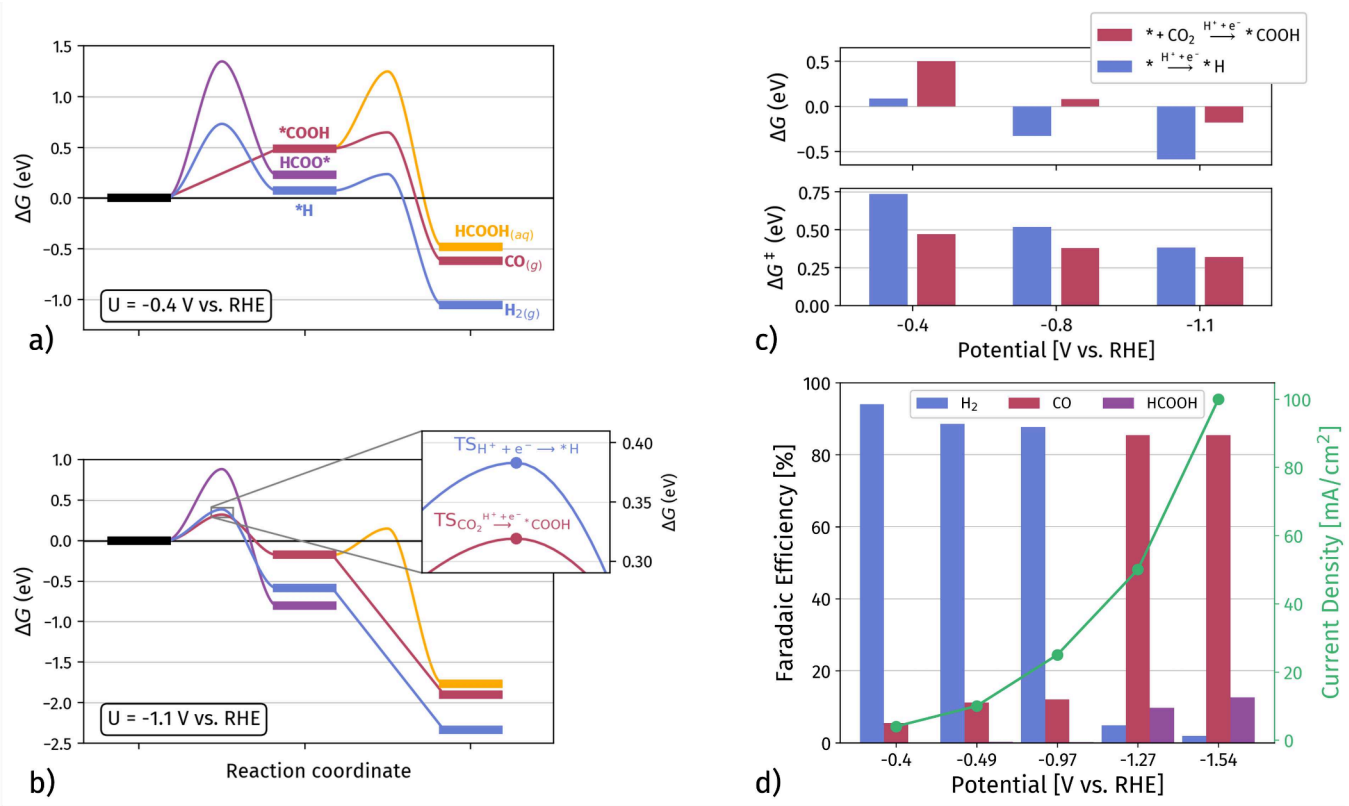


Figure 5. (a) and (b): Grand-canonical free energy variations ΔG on Ag(111) along CO_2RR and HER at $U = -0.4$ V vs RHE (a) and $U = -1.1$ V vs RHE (b). The inset in panel (b) shows a zoom on the activation grand-canonical free energies of *H production in HER (blue line) and *COOH formation in CO_2RR. (c) Comparison of reaction (upper panel) and activation (lower panel) grand canonical free energies for reaction steps in eqs 1 (red bars) and (5) (blue bars). (d) Experimental FEs of CO_2RR to CO (red bars) or to HCOOH (purple bars) and HER (blue bars) of a synthesized polycrystalline Ag electrocatalyst in a pH 2 electrolyte.

https://doi.org/10.1021/acs.jpclett.4c02869
J. Phys. Chem. Lett. 2024, 15, 11538−11545

−0.4, − 0.8, − 1.1 V vs RHE, are reported in Figure 4. Comparing the activation grand-canonical energies, it appears that for CO_2RR the formation of $HCOO^-$ via reaction mechanism (8) enjoys the lowest kinetic barriers on all investigated silver surfaces. On the contrary, the PCET mechanism favors the formation of the *COOH intermediate, while the activation energy for the formation of HCOO* remains higher than 0.5 eV on all surfaces at all studied potentials. Consequently, considering PCET mechanisms, CO_2RR tends to proceed through the *COOH intermediate, eq 1, followed by CO production, eq 2, which has much lower barriers than the step in eq 9, forming HCOOH. Finally, the mechanism in eq 7 exhibits the highest activation energies on all silver surfaces, indicating that this reaction pathway is highly disfavored. Considering HER, the Volmer step in eq 5 exhibits a decreasing activation barrier from approximately 1.0 eV at −0.4 V vs RHE to around 0.4 eV when the cathodic potential is lowered to −1.1 V vs RHE. Once hydrogen is adsorbed, the Heyrovsky reaction in eq 6 proceeds with very low activation energies across the entire potential range, becoming barrierless on Ag(100) and Ag(111) at potentials lower than about −0.8 V vs RHE. The Volmer step of HER is therefore quickly followed by the Heyrovsky step, producing H_2, rather than the CO_2RR step in eq 8, where the adsorbed hydrogen from the Volmer step reacts with CO_2 to form $HCOO^-$. Globally then, the suppressed production of formate on Ag can be attributed to two main factors. First, the high kinetic barrier for HCOO* formation via the PCET in eq 3. Second, the very low *H coverage,[27] resulting from high hydrogen adsorption energy and low Heyrovsky activation energy, which hinders the direct $HCOO^-$ formation via eq 8. From the activation grand-canonical energies in Figure 4 we can then conclude that on silver surfaces the CO_2RR proceeds to CO along the PCET steps in eqs 1, (2), passing through the *COOH intermediate. In competition, silver also produces hydrogen through the Volmer-Heyrovsky mechanism. All other pathways appear to be comparatively disfavored. From the analysis of $\Delta\Omega^{\ddagger}$ of HER and CO_2RR, we may conclude that the latter is the most kinetically favored reduction reaction on all silver surfaces, across the whole potential window. However, this finding contradicts the experimental evidence mentioned in the introduction, which indicates a predominant HER at low overpotential.

To obtain a complete and comprehensive description of the reaction mechanisms, it is then essential to consider both thermodynamics and kinetics together. Due to the similar thermodynamic and kinetic results, we focus on the Ag(111) surface. In Figure 5a,b we report the variation in grand-canonical free energy, ΔG, along HER and CO_2RR, including intermediate and transition states. Reaction grand-canonical free energies are computed at constant applied potential, employing the described hybrid explicit-implicit solvation setup. Activation grand-canonical free energies, $\Delta G^{\ddagger}$, are derived from the grand-canonical energies of the transition states found with constant-potential calculations. In the calculation of grand-canonical free energies we consider hydronium ions in equilibrium in bulk water. Grand-canonical free energies and activation free energies at U = −0.4, − 0.8− 1.1 V vs RHE are also reported in Figure 5c.

At low overpotential, U = −0.4 V vs RHE, as shown in Figure 5a, the states with the highest grand-canonical free energies, when considering full ΔG variations along the CO_2RR pathways, are the TSs of HCOO* formation, eq 3, purple line, and HCOOH formation from *COOH, eq 9, yellow line. Interestingly, for the *COOH formation, eq 1, red line, it is the intermediate *COOH that shows the highest grand-canonical free energy. This can also be seen in Figure 5c. Here, at U = −0.4 V vs RHE, the activation grand-canonical free energy $\Delta G^{\ddagger}$ of *COOH production (red bar in the lower panel), computed from the grand-canonical electronic energy of the TS, is lower than the reaction grand-canonical free energy ΔG (red bar, upper panel). Hence, no actual kinetic barrier appear along the grand-canonical free energy reaction path in Figure 5a. In this situation, the backward step, $CO_2 \leftarrow$ *COOH, is then both thermodynamically favored and kinetically barrierless. Consequently, at low overpotential, CO_2RR is overall suppressed: the production of *COOH is hindered by the unfavorable thermodynamics, while the formation of HCOO* is prevented by the large kinetic barrier. In this range of applied voltage, HER dominates, even though the $\Delta G^{\ddagger}$ of the Volmer step remains above 0.5 eV, in line with the value of $\Delta\Omega^{\ddagger}$ in Figure 4. As the bias is lowered to U = −1.1 V vs RHE, Figure 5b, the intermediate state *COOH is stabilized, its grand-canonical free energy of formation becomes lower and a kinetic barrier emerges, see also Figure 5c. *COOH can then be formed and further reduced to CO without kinetic barrier. At the same time, HCOOH formation from *COOH still shows a nonzero activation energy, making this step less favorable. Most importantly, as highlighted in the inset of Figure 5b, the kinetic barrier for *COOH formation is lower than that of the Volmer step of HER, resulting in a more favorable CO production compared to H_2. Therefore, at intermediate potentials the selectivity switches from HER to CO_2RR, specifically with almost only CO production.

To validate our theoretical investigations, focusing specifically on reaction steps involving hydronium ions as proton donors, we carried out electrochemical characterizations of silver electrodes in an acidic environment. Indeed, most CO_2RR experiments in the literature were performed at neutral or alkaline pH, and the acidic reaction has received minor attention.[61,62] A polycrystalline silver electrode was prepared via sputtering,[38] and tested in flow cell with an electrolyte at pH 2. More details about the experimental procedure are reported in the Supporting Information. As shown in Figure 5c, CO and H_2 emerge as the primary gaseous products, with small amounts of HCOOH. The expected trend is clearly observable: a shift from HER, favored up to intermediate potentials of about −1 V vs RHE, to CO production at more negative potentials, accompanied by an increase in the current density. The cumulative FE values for CO, H_2, and HCOOH approximate 100%, suggesting minimal formation of other products. These results are in good agreement with our proposed theoretical model which predicts a selectivity switch at around the same applied potential values.

We conclude that, in critical cases such as the reactions investigated on silver electrodes, simpler or partial approaches may fail to provide a correct and complete understanding of the reaction mechanisms. In these situations, only by integrating the theoretical estimation of both reaction thermodynamics and kinetics we can obtain a detailed and satisfactory explanation of the observed selectivity in CO_2RR. Our focus on the case study of Ag electrocatalysts demonstrates that comprehensive DFT modeling is essential to reliably understand the underlying mechanisms of electrochemical reactions and derive meaningful predictions.

https://doi.org/10.1021/acs.jpclett.4c02869
J. Phys. Chem. Lett. 2024, 15, 11538−11545

■ ASSOCIATED CONTENT

Supporting Information

The Supporting Information is available free of charge at https://pubs.acs.org/doi/10.1021/acs.jpclett.4c02869.

Computational Details: DFT setup and Thermodynamics and Kinetics, Detailed Explanation of Reaction Mechanisms, and Geometries of Transition States (PDF)

■ AUTHOR INFORMATION

Corresponding Author

Hannes Jónsson − *Science Institute and Faculty of Physical Sciences, University of Iceland, 107 Reykjavík, Iceland; Department of Chemistry, Brown University, Providence, Rhode Island 02912, United States;* orcid.org/0000-0001-8285-5421; Email: hj@hi.is

Authors

Michele Re Fiorentin − *Department of Applied Science and Technology, Politecnico di Torino, 10129 Torino, Italy;* orcid.org/0000-0002-1074-0411

Francesca Risplendi − *Department of Applied Science and Technology, Politecnico di Torino, 10129 Torino, Italy;* orcid.org/0000-0002-1277-6733

Clara Salvini − *Department of Applied Science and Technology, Politecnico di Torino, 10129 Torino, Italy;* orcid.org/0000-0002-8451-7896

Juqin Zeng − *Department of Applied Science and Technology, Politecnico di Torino, 10129 Torino, Italy;* orcid.org/0000-0001-8885-020X

Giancarlo Cicero − *Department of Applied Science and Technology, Politecnico di Torino, 10129 Torino, Italy;* orcid.org/0000-0002-2920-9882

Complete contact information is available at: https://pubs.acs.org/10.1021/acs.jpclett.4c02869

Author Contributions

†MRF and FR contributed equally to this work.

Notes

The authors declare no competing financial interest.

■ ACKNOWLEDGMENTS

MRF, FR and GC acknowledge the High-Performance Computing, Big Data, and Quantum Computing Research Centre, established under the Italian National Recovery and Resilience Plan (PNRR). We acknowledge financial support under the National Recovery and Resilience Plan (NRRP), Mission 4, Component 2, Investment 1.1, Call for tender No. 104 published on 2.2.2022 by the Italian Ministry of University and Research (MUR), funded by the European Union − NextGenerationEU − Project Title: A Combined Experimental and Theoretical Approach for Single-Atom Catalyst Engineering Towards Tuneable Activity and Selectivity in CO2 electroreduction (RECYCLE-CO2) - Grant Assignment Decree No. 2022FM3LXT, and from the Icelandic Research Fund (no. 207283-053).

■ REFERENCES

(1) Mac Dowell, N.; Fennell, P. S.; Shah, N.; Maitland, G. C. The role of CO2 capture and utilization in mitigating climate change. *Nature Climate Change* **2017**, *7*, 243−249.

(2) Dibenedetto, A.; Angelini, A.; Stufano, P. Use of carbon dioxide as feedstock for chemicals and fuels: homogeneous and heterogeneous catalysis. *J. Chem. Technol. Biotechnol.* **2014**, *89*, 334−353.

(3) Tomboc, G. M.; Choi, S.; Kwon, T.; Hwang, Y. J.; Lee, K. Potential Link between Cu Surface and Selective CO2 Electroreduction: Perspective on Future Electrocatalyst Designs. *Adv. Mater.* **2020**, *32*, 1908398.

(4) Ma, Y.; Wang, J.; Yu, J.; Zhou, J.; Zhou, X.; Li, H.; He, Z.; Long, H.; Wang, Y.; Lu, P.; Yin, J.; Sun, H.; Zhang, Z.; Fan, Z. Surface modification of metal materials for high-performance electrocatalytic carbon dioxide reduction. *Matter* **2021**, *4*, 888−926.

(5) Wang, Y.; Liu, Y.; Liu, W.; Wu, J.; Li, Q.; Feng, Q.; Chen, Z.; Xiong, X.; Wang, D.; Lei, Y. Regulating the coordination structure of metal single atoms for efficient electrocatalytic CO2 reduction. *Energy Environ. Sci.* **2020**, *13*, 4609−4624.

(6) Hu, X.-M.; Hval, H. H.; Bjerglund, E. T.; Dalgaard, K. J.; Madsen, M. R.; Pohl, M.-M.; Welter, E.; Lamagni, P.; Buhl, K. B.; Bremholm, M.; Beller, M.; Pedersen, S. U.; Skrydstrup, T.; Daasbjerg, K. Selective CO2 Reduction to CO in Water using Earth-Abundant Metal and Nitrogen-Doped Carbon Electrocatalysts. *ACS Catal.* **2018**, *8*, 6255−6264.

(7) Wang, X.; Ju, W.; Liang, L.; Riyaz, M.; Bagger, A.; Filippi, M.; Rossmeisl, J.; Strasser, P. Electrochemical CO2 Activation and Valorization on Metallic Copper and Carbon-Embedded N-Coordinated Single Metal MNC Catalysts. *Angew. Chem., Int. Ed.* **2024**, *63*, e202401821.

(8) Vavra, J.; Ramona, G. P. L.; Dattila, F.; Kormányos, A.; Priamushko, T.; Albertini, P. P.; Loiudice, A.; Cherevko, S.; Lopéz, N.; Buonsanti, R. Solution-based Cu+ transient species mediate the reconstruction of copper electrocatalysts for CO2 reduction. *Nature Catalysis* **2024**, *7*, 89−97.

(9) Zhang, T.; Lu, X.; Qi, W.; Qin, G.; Li, S. Efficient electroreduction of CO2 to CO on silver single-atom catalysts: Activity enhancement through coordinated modulation of polyaniline. *Applied Catalysis B: Environment and Energy* **2024**, *349*, 123896.

(10) Zhao, Z.; Lin, L.; Ni, Y.; Jin, L.; Feng, L.; Wang, Y.; Wei, Y.; Zhang, J.; Chen, J. Atomic level dispersed nickel coupled with silver nanoparticle to boost the efficiency of CO2 conversion to CO via spin electrons regulation. *Applied Catalysis B: Environment and Energy* **2024**, *349*, 123886.

(11) Singh, M. R.; Clark, E. L.; Bell, A. T. Effects of electrolyte, catalyst, and membrane composition and operating conditions on the performance of solar-driven electrochemical reduction of carbon dioxide. *Phys. Chem. Chem. Phys.* **2015**, *17*, 18924−18936.

(12) Wagner, A.; Sahm, C. D.; Reisner, E. Towards molecular understanding of local chemical environment effects in electro- and photocatalytic CO2 reduction. *Nature Catalysis* **2020**, *3*, 775−786.

(13) Pan, F.; Yang, Y. Designing CO2 reduction electrode materials by morphology and interface engineering. *Energy Environ. Sci.* **2020**, *13*, 2275−2309.

(14) Yu, Q.; Guo, C.; Ge, J.; Zhao, Y.; Liu, Q.; Gao, P.; Xiao, J.; Li, H. Morphology controlling of silver by plasma engineering for electrocatalytic carbon dioxide reduction. *J. Power Sources* **2020**, *453*, 227846.

(15) Luc, W.; Collins, C.; Wang, S.; Xin, H.; He, K.; Kang, Y.; Jiao, F. Ag-Sn Bimetallic Catalyst with a Core-Shell Structure for CO2 Reduction. *J. Am. Chem. Soc.* **2017**, *139* (5), 1885−1893.

(16) de Salles Pupo, M. M.; Kortlever, R. Electrolyte Effects on the Electrochemical Reduction of CO2. *ChemPhysChem* **2019**, *20*, 2926−2935.

(17) Marcandalli, G.; Monteiro, M. C. O.; Goyal, A.; Koper, M. Electrolyte Effects on CO2 Electrochemical Reduction to CO. *Acc. Chem. Res.* **2022**, *55*, 1900−1911.

(18) Sa, Y. J.; Lee, C. W.; Lee, S. Y.; Na, J.; Lee, U.; Hwang, Y. J. Catalyst−electrolyte interface chemistry for electrochemical CO2 reduction. *Chem. Soc. Rev.* **2020**, *49*, 6632−6665.

(19) Varela, A.; Kroschel, M.; Leonard, N.; Ju, W.; Steinberg, J.; Bagger, A.; Rossmeisl, J.; Strasser, P. pH Effects on the Selectivity of the Electrocatalytic CO2 Reduction on Graphene-Embedded Fe−N−

C Motifs: Bridging Concepts between Molecular Homogeneous and Solid-State Heterogeneous Catalysis. *ACS energy letters* **2018**, *3*, 812−817.
(20) Song, H.; Song, J.; Kim, B.; Tan, Y.; Oh, J. Activation of C2H4 reaction pathways in electrochemical CO2 reduction under low CO2 partial pressure. *Appl. Catal., B* **2020**, *272*, 119049.
(21) Tufa, R. A.; Chanda, D.; Ma, M.; Aili, D.; Demissie, T.; Vaes, J.; Li, Q.; Liu, S.; Pant, D. Towards highly efficient electrochemical CO2 reduction: Cell designs, membranes and electrocatalysts. *Applied Energy* **2020**, *277*, 115557.
(22) Nørskov, J. K.; Rossmeisl, J.; Logadottir, A.; Lindqvist, L.; Kitchin, J. R.; Bligaard, T.; Jónsson, H. Origin of the Overpotential for Oxygen Reduction at a Fuel-Cell Cathode. *J. Phys. Chem. B* **2004**, *108*, 17886−17892.
(23) Montoya, J. H.; Seitz, L. C.; Chakthranont, P.; Vojvodic, A.; Jaramillo, T. F.; Nørskov, J. K. Materials for solar fuels and chemicals. *Nat. Mater.* **2017**, *16*, 70−81.
(24) Skúlason, E.; Jónsson, H. Atomic scale simulations of heterogeneous electrocatalysis: recent advances. *Advances in Physics: X* **2017**, *2*, 481−495.
(25) Kulkarni, A.; Siahrostami, S.; Patel, A.; Nørskov, J. K. Understanding Catalytic Activity Trends in the Oxygen Reduction Reaction. *Chem. Rev.* **2018**, *118*, 2302−2312.
(26) Singh, M. R.; Goodpaster, J. D.; Weber, A. Z.; Head-Gordon, M.; Bell, A. T. Mechanistic insights into electrochemical reduction of CO_2 over Ag using density functional theory and transport models. *Proc. Natl. Acad. Sci. U. S. A.* **2017**, *114*, E8812−E8821.
(27) Hussain, J.; Jónsson, H.; Skúlason, E. Calculations of Product Selectivity in Electrochemical CO2 Reduction. *ACS Catal.* **2018**, *8*, 5240−5249.
(28) Van den Bossche, M.; Skúlason, E.; Rose-Petruck, C.; Jónsson, H. Addition to "Assessment of Constant-Potential Implicit Solvation Calculations of Electrochemical Energy Barriers for H2 Evolution on Pt. *J. Phys. Chem. C* **2019**, *123*, 15875−15875.
(29) Van den Bossche, M.; Rose-Petruck, C.; Jónsson, H. Competing HCOOH and CO Pathways in CO2 Electroreduction at Copper Electrodes: Calculations of Voltage-Dependent Activation Energy. *J. Phys. Chem. C* **2021**, *125*, 13802−13808.
(30) Govindarajan, N.; Xu, A.; Chan, K. How pH affects electrochemical processes. *Science* **2022**, *375*, 379−380.
(31) Ma, M.; Deng, W.; Xu, A.; Hochfilzer, D.; Qiao, Y.; Chan, K.; Chorkendorff, I.; Seger, B. Local reaction environment for selective electroreduction of carbon monoxide. *Energy Environ. Sci.* **2022**, *15*, 2470−2478.
(32) Kastlunger, G.; Wang, L.; Govindarajan, N.; Heenen, H. H.; Ringe, S.; Jaramillo, T.; Hahn, C.; Chan, K. Using pH Dependence to Understand Mechanisms in Electrochemical CO Reduction. *ACS Catal.* **2022**, *12*, 4344−4357.
(33) Karmodak, N.; Vijay, S.; Kastlunger, G.; Chan, K. Computational Screening of Single and Di-Atom Catalysts for Electrochemical CO2 Reduction. *ACS Catal.* **2022**, *12*, 4818−4824.
(34) Dinh, C.-T.; García de Arquer, F. P.; Sinton, D.; Sargent, E. H. High Rate, Selective, and Stable Electroreduction of CO2 to CO in Basic and Neutral Media. *ACS Energy Letters* **2018**, *3*, 2835−2840.
(35) Van den Hoek, J.; Daems, N.; Arnouts, S.; Hoekx, S.; Bals, S.; Breugelmans, T. Improving Stability of CO2 Electroreduction by Incorporating Ag NPs in N-Doped Ordered Mesoporous Carbon Structures. *ACS Appl. Mater. Interfaces* **2024**, *16*, 6931−6947.
(36) Qin, Y.; Zhan, G.; Tang, C.; Yang, D.; Wang, X.; Yang, J.; Mao, C.; Hao, Z.; Wang, S.; Qin, Y.; Li, H.; Chen, K.; Liu, M.; Li, J. Homogeneous Vacancies-Enhanced Orbital Hybridization for Selective and Efficient CO2-to-CO Electrocatalysis. *Nano Lett.* **2023**, *23*, 9227−9234.
(37) Fortunati, A.; Risplendi, F.; Re Fiorentin, M.; Cicero, G.; Parisi, E.; Castellino, M.; Simone, E.; Iliev, B.; Schubert, T. J. S.; Russo, N.; Hernández, S. Understanding the role of imidazolium-based ionic liquids in the electrochemical CO2 reduction reaction. *Communications Chemistry* **2023**, *6*, 84.
(38) Monti, N. B. D.; Fontana, M.; Sacco, A.; Chiodoni, A.; Lamberti, A.; Pirri, C. F.; Zeng, J. Facile Fabrication of Ag Electrodes for CO2-to-CO Conversion with Near-Unity Selectivity and High Mass Activity. *ACS Applied Energy Materials* **2022**, *5*, 14779−14788.
(39) Hoshi, N.; Kato, M.; Hori, Y. Electrochemical reduction of CO2 on single crystal electrodes of silver Ag(111), Ag(100) and Ag(110). *J. Electroanal. Chem.* **1997**, *440*, 283−286.
(40) Hatsukade, T.; Kuhl, K. P.; Cave, E. R.; Abram, D. N.; Jaramillo, T. F. Insights into the electrocatalytic reduction of CO2 on metallic silver surfaces. *Phys. Chem. Chem. Phys.* **2014**, *16*, 13814−13819.
(41) Dutta, A.; Morstein, C. E.; Rahaman, M.; Cedeño López, A.; Broekmann, P. Beyond Copper in CO2 Electrolysis: Effective Hydrocarbon Production on Silver-Nanofoam Catalysts. *ACS Catal.* **2018**, *8*, 8357−8368.
(42) Clark, E. L.; Ringe, S.; Tang, M.; Walton, A.; Hahn, C.; Jaramillo, T. F.; Chan, K.; Bell, A. T. Influence of Atomic Surface Structure on the Activity of Ag for the Electrochemical Reduction of CO2 to CO. *ACS Catal.* **2019**, *9*, 4006−4014.
(43) Kresse, G.; Hafner, J. Ab initio molecular dynamics for liquid metals. *Phys. Rev. B* **1993**, *47*, 558−561.
(44) Kresse, G.; Hafner, J. Ab initio molecular-dynamics simulation of the liquid-metal-amorphous-semiconductor transition in germanium. *Phys. Rev. B* **1994**, *49*, 14251−14269.
(45) Kresse, G.; Furthmüller, J. Efficiency of ab-initio total energy calculations for metals and semiconductors using a plane-wave basis set. *Comput. Mater. Sci.* **1996**, *6*, 15−50.
(46) Kresse, G.; Furthmüller, J. Efficient iterative schemes for ab initio total-energy calculations using a plane-wave basis set. *Phys. Rev. B* **1996**, *54*, 11169−11186.
(47) Blöchl, P. E. Projector augmented-wave method. *Phys. Rev. B* **1994**, *50*, 17953−17979.
(48) Hammer, B.; Hansen, L. B.; Nørskov, J. K. Improved adsorption energetics within density-functional theory using revised Perdew-Burke-Ernzerhof functionals. *Phys. Rev. B* **1999**, *59*, 7413−7421.
(49) Monkhorst, H. J.; Pack, J. D. Special points for Brillouin-zone integrations. *Phys. Rev. B* **1976**, *13*, 5188−5192.
(50) Pack, J. D.; Monkhorst, H. J. Special points for Brillouin-zone integrations"—a reply. *Phys. Rev. B* **1977**, *16*, 1748−1749.
(51) Gunceler, D.; Letchworth-Weaver, K.; Sundararaman, R.; Schwarz, K. A.; Arias, T. A. The importance of nonlinear fluid response in joint density-functional theory studies of battery systems. *Modell. Simul. Mater. Sci. Eng.* **2013**, *21*, 074005.
(52) Mathew, K.; Kolluru, V. S. C.; Hennig, R. G. VASPsol: Implicit solvation and electrolyte model for density-functional theory. https://github.com/henniggroup/VASPsol, accessed on 07−2022.
(53) Mathew, K.; Sundararaman, R.; Letchworth-Weaver, K.; Arias, T. A.; Hennig, R. G. Implicit solvation model for density-functional study of nanocrystal surfaces and reaction pathways. *J. Chem. Phys.* **2014**, *140*, 084106.
(54) Mathew, K.; Kolluru, V. S. C.; Mula, S.; Steinmann, S. N.; Hennig, R. G. Implicit self-consistent electrolyte model in plane-wave density-functional theory. *J. Chem. Phys.* **2019**, *151*, 234101.
(55) Henkelman, G.; Jónsson, H. A dimer method for finding saddle points on high dimensional potential surfaces using only first derivatives. *J. Chem. Phys.* **1999**, *111*, 7010−7022.
(56) Olsen, R. A.; Kroes, G. J.; Henkelman, G.; Arnaldsson, A.; Jónsson, H. Comparison of methods for finding saddle points without knowledge of the final states. *J. Chem. Phys.* **2004**, *121*, 9776−9792.
(57) Plasencia Gutiérrez, M.; Argáez, C.; Jónsson, H. Improved Minimum Mode Following Method for Finding First Order Saddle Points. *J. Chem. Theory Comput.* **2017**, *13*, 125−134.
(58) Smidstrup, S.; Pedersen, A.; Stokbro, K.; Jónsson, H. Improved initial guess for minimum energy path calculations. *J. Chem. Phys.* **2014**, *140*, 214106.
(59) Rosen, J.; Hutchings, G. S.; Lu, Q.; Rivera, S.; Zhou, Y.; Vlachos, D. G.; Jiao, F. Mechanistic Insights into the Electrochemical

Reduction of CO2 to CO on Nanostructured Ag Surfaces. *ACS Catal.* **2015**, *5*, 4293−4299.
(60) Yoo, J. S.; Christensen, R.; Vegge, T.; Nørskov, J. K.; Studt, F. Theoretical Insight into the Trends that Guide the Electrochemical Reduction of Carbon Dioxide to Formic Acid. *ChemSusChem* **2016**, *9*, 358−363.
(61) Yu, J.; Xiao, J.; Ma, Y.; Zhou, J.; Lu, P.; Wang, K.; Yan, Y.; Zeng, J.; Wang, Y.; Song, S.; Fan, Z. Acidic conditions for efficient carbon dioxide electroreduction in flow and MEA cells. *Chem. Catalysis* **2023**, *3*, 100670.
(62) Zhang, B.; Zou, J.; Chen, Z.; Yan, W.; Liu, W.; Dong, C.; Cai, D.; Zhang, Q.; Wang, Y.; Xie, S. Defect-engineered carbon-confined silver for enhanced CO2 electrocatalytic reduction to CO in acidic media. *Next Nanotechnology* **2023**, *2*, 100014.

https://doi.org/10.1021/acs.jpclett.4c02869
J. Phys. Chem. Lett. 2024, 15, 11538−11545